Microseismicity along Xiaojiang Fault Zone (China) and the Characterization of Interseismic Fault Behavior

Yijian Zhou[1,2*], Han Yue[1*], Shiyong Zhou[1], Lihua Fang[3], Yun Zhou[3], Lisheng Xu[3], Ziming Liu[1], Teng Wang[1], Li Zhao[1], Abhijit Ghosh[2]

[1]Institute of Theoretical and Applied Geophysics, Peking University, Beijing, China.

[2]Department of Earth Sciences, University of California, Riverside, California, USA

[3]Institute of Geophysics, China Earthquake Administration, Beijing, China

Corresponding author:

Yijian Zhou (yijian.zhou@email.ucr.edu)

Han Yue (yue.han@pku.edu.cn)

Key Points:

- We obtained a high-resolution interseismic catalog (2016-2019) near the Xiaojiang Fault Zone.
- Widespread microseismicity are detected on off-fault structures, but the major fault shows low seismicity.
- Seismicity behavior reveals slip and strength pattern of Xiaojiang Fault and off-fault branches.

Abstract

The Xiaojiang Fault (XJF) Zone locates in the southeastern of Tibetan Plateau and defines the boundary between the South China and Sichuan-Yunnan blocks. Historical large earthquakes were hosted on the XJF, though its seismic hazard in the near future is under debate. In this study, we utilize portable broad-band seismic network to unravel the microseismic activities along XJF, and to further investigate the fault structures and their properties. Adopting PALM, a newly developed earthquake detection algorithm, we obtained ~13,000 relocated events. The micro-seismicity reveals widespread off-fault structures showing conjugate geometry, while the major faults present low seismicity. The fault branches conjugate to the main-fault present intensive microseismicity, which hosts repeating events and presents high b-value. Regional GPS stations reflect slips are mostly concentrated along the XJF, while the slip rate on off-fault branches correlates with seismic activities on these structures. Combining with other recent seismological and magnetotellurics evidences, we suggest a low strength on these off-fault structures, which may partially release tectonic stress loading and serve as a barrier for future big earthquakes. On the XJF, the microseismic events are clustered on the fault junctions with low b-value. A special set of clusters between 25°N to 25.5°N show an along-strike variation of depth from 10 to 25-km, imaging the boundary between creeping and locked fault portions. We revisit the seismic hazard problem of XJF, and conclude that XJF is at the late stage of inter-seismic period.

Plain Language Summary

The Xiaojiang Fault (XJF) Zone locates in the southeastern of Tibetan Plateau and is considered as an active block boundary. The seismic hazard of XJF is of public importance because of the active large earthquakes in the history, though it is under debate. In this study, we utilize temporary seismic network to detect small earthquakes (i.e., microseismicity) along XJF, and to further infer the fault structures and their properties. We finally obtained ~13,000 events with well-constraint location. We find that off-fault structures have intense microseismicity, while the major faults present quiescent behavior. We made detailed analysis on the seismicity and suggest a low strength on these off-fault structures, which may partially release tectonic stress loading and serve as a barrier for future big earthquakes. On the XJF, the microseismic events are clustered on the fault junctions with low b-value that indicate high stress level. We revisit the seismic hazard problem of XJF, and conclude that XJF is at the late stage of inter-seismic period.

1. Introduction

1.1 The Tectonic Background and Seismic Hazard

The Xiaojiang Fault (XJF) is located in the southeastern margin of the Tibetan Plateau, which defines the displacement boundary between the South China block in the east and the Sichuan-Yunnan block in the west (Figure 1). The fault zone stretches for about 400-km in the north-south direction (Shen et al., 2003; Zhang et al., 2003). Driven by the eastward extension of the Tibetan Plateau, the rhombic Sichuan-Yunnan block moves southeastward relative to the stable South China block at a rate of 7-10 mm/yr, accompanied by a clockwise rotation (Shen et al., 2005; Wang et al., 2015; Fu et al., 2020). Strong earthquakes are active along the eastern boundary of the Sichuan-Yunnan block, which is composed of the Xianshuihe Fault (XSHF), the Anninghe-Zemuhe Fault (AZF), and the Xiaojiang Fault (Figure 1, (Deng et al., 2003b; Zhang et al., 2003). Historical earthquakes on XJF include three M7~8 and sixteen M6~7 events that occurred since 1500 A.D. (Wen et al., 2008; Ren, 2013), with the largest and latest two being the 1833 M8 Songming and the 1733 M7.5 Dongchuan earthquake. The ~200-year quiescence and long-term active behavior of large earthquake on XJF make the seismic hazard assessment of great scientific and public importance. Thus, special focus has been placed on monitoring the seismic activities, e.g., the China Seismic Experimental Sites (CSES, (Wu et al., 2019) and studying the fault behavior of the Xiaojiang fault area. However, previous studies have not reach agreement on the seismic hazard of XJF:

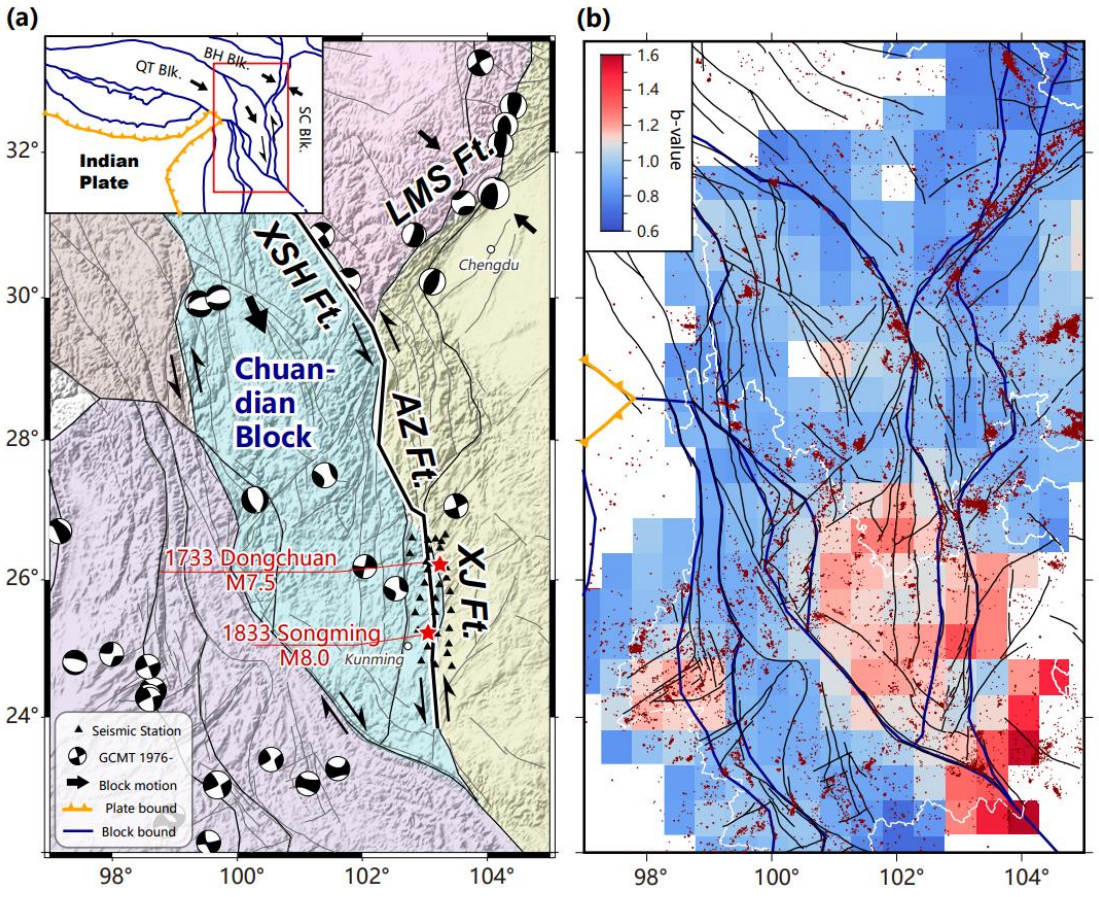

Figure 1. (a) Tectonic setting of the Sichuan-Yunnan block. Active tectonic blocks are marked by colored patches. The horizontal movement of the blocks is indicated by gray arrows. Fault traces are plotted in gray lines. The Xianshuihe Fault (XSH Ft.), Anninghe-Zemuhe Fault (AZ Ft.), and Xiaojiang Fault (XJ Ft.) are highlighted by black lines. The focal spheres are solutions in the region since 1976 from the GCMT catalog. The black triangles denote broadband seismic stations used in this study (see Figure 2 for details). In the inset map, the red box indicates the study region. Blue lines show boundaries of tectonic blocks, while plate boundaries are marked by orange lines with ticks. (b) Seismicity and b-value of the study region. The background color shows the b-value, whereas red dots are epicenters of seismic events of magnitude 1.5-7.0 during 2016-2019 from the regional catalog of CSES.

Adopting a simple earthquake recurrence model, the seismic hazard can be estimated by the elapsed time from the preceding large earthquake, while the near future seismic hazard along the XJF is under debate. Historical earthquakes on XJF show an irregular recurrence interval and magnitude for M6~7 events (Wen et al., 2008), while paleoseismic studies find characteristic earthquakes of M>7.5, whose recurrence interval is about 2000 years (Shen and Wang, 1999; Shen et al., 2003). However, a recent paleo-seismic study by Li et al. (2015) found a much shorter recurrence interval of 370-480 years for the characteristic events on the western branch of XJF. Based on these observations, Liu et al. (2020) propose a high probability of an M>7 event on XJF in the near future.

Geodetic measurements provide another independent observation to estimate earthquake hazard. Wang et al. (2015) calculated the balance between the GPS measured tectonic loading and the strain release by historical earthquakes, which gives a high moment deficit on XJF indicating high potential of large earthquakes; whereas using a similar approach, Wang et al. (2011) obtained a negative moment deficit, which indicates a low potential of large earthquakes. It appears that the discrepancy of seismic hazard originates from the different remnant stress assumed by different groups.

Besides paleo-seismic and geodetic evidence, the current stress status is another probe to assess the possibility of a near-future earthquake. This can be inferred from b-value distribution (see Section 1.2, (Scholz, 1968; Gulia et al., 2018; Gulia and Wiemer, 2019), which avoids the problem of an uncertain residual stress in the aforementioned geodetic method. We mapped b-value distribution in the Chuandian region with a regional earthquake catalog (see Section 3.5 for the calculation of b-value). It turned out that XJF has a relatively high b-value, which may be associated with low stress level, in comparison with AZF and XSHF that located to the north (Figure 1b).

Overall, the discrepancies in previous studies are probably induced from low-resolution observations, which prevent discussions on the factors that control the initiation and propagation of rupture, including the fault geometry, coupling state, stress and strength distribution etc.

1.2 Microseismicity Analysis

Microseismic activities can be used to resolve the fine structure of fault zones, and to investigate multiple attributes of the fault properties, including its slip behavior and stress level. The imaging of fault structural features at seismogenic depth is a direct outcome of high-resolution event location (Waldhauser and Ellsworth, 2002; Shelly et al., 2016; Mendoza et al., 2019). For example, utilizing relocated aftershocks to constrain the fault geometry has become a common practice in investigating kinematic rupture processes of large earthquakes (Shelly et al., 2016; Yue et al., 2017; Melgar et al., 2018; Sun et al., 2018).

The aseismic slip behaviors of faults can be indicated by repeating earthquakes, which is generally interpreted as the repeating rupture of isolated asperities loaded by surrounding fault creeping (Uchida and Bürgmann, 2019). Repeaters are often observed in the peripheries of co-seismic rupture zones (Templeton et al., 2009; Chen et al., 2010; Uchida and Matsuzawa, 2011) and the boundaries of locking sections on the fault planes (Bürgmann et al., 2000; Uchida et al., 2009; Chaussard et al., 2015). Strictly detected repeaters that have quasi-periodic recurrence intervals can be used to estimate slip rates at seismogenic depth, which may be beyond the resolution of geodetic observations (Uchida, 2019).

The frequency-magnitude distribution (FMD) is commonly found to be a power-law distribution, i.e. the Gutenberg-Richter law (G-R law, (Gutenberg and Richter, 1944). The b-value is the slope of FMD, which evaluates the number ratio between

large and small events, and is found to be related to the stress status. The anti-correlation between the b-value and stress level was first discovered in rock experiments (Scholz, 1968), and is further validated by a series of statistical analyses on the correlations between the b-value and focal depths (Mori and Abercrombie, 1997; Spada et al., 2013), focal mechanism (Schorlemmer et al., 2005), and pore pressure in injection-induced seismicity (Bachmann et al., 2012). These studies demonstrated that an anti-correlation between the b-value and deviatoric stress also applies to natural faults. Thus, asperities that accumulate high levels of stress can be mapped by areas of low b-values (Wiemer and Wyss, 1997; Wyss et al., 2000; Schorlemmer and Wiemer, 2005; Ghosh et al., 2008; Tormann et al., 2014).

In this study, we adopt micro-seismic activity to resolve the fault zone properties and to estimate the seismic hazard on XJF. To construct a high-resolution seismic catalog, we deploy temporary seismic stations and apply a newly developed earthquake detection method. Based on the catalog, we perform spatiotemporal analysis, detect repeaters, and map the b-value, with the purpose to infer the fault structure and strength, slip behavior, and stress status of XJF.

2. Data and Methods

2.1 Regional Networks and Data

We use continuous data from 31 broadband seismic stations along the main segment of XJF involving two sub-parallel traces of faults (Figure 2). The network is composed of two sub-arrays deployed by different groups, which respectively includes 20 and 11 stations, respectively. The network has an average inter-station distance of 20-30km. The network was operated from September 2016 to January 2019, with a daily average of about 80% of the stations in operation (Figure S1).

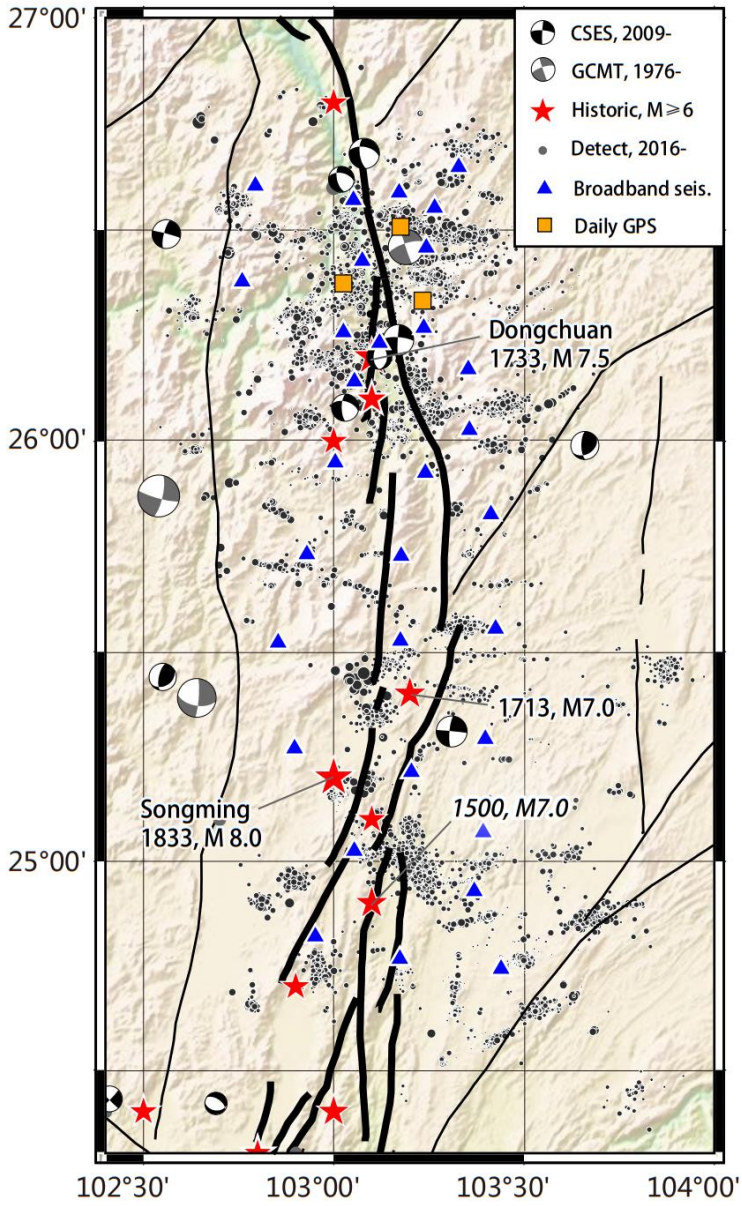

Figure 2. Seismic stations along the XJF used in this study. Blue triangles denote broadband stations; orange squares denote daily GPS stations. Black dots are the detected micro-seismic events. Historical earthquakes of magnitudes M ≥ 6 are denoted by red stars. Focal mechanism solutions from the GCMT catalog since 1976 and the CSES catalog since 2009 are shown by gray and black focal spheres, respectively. Black lines depict active faults, and that of XJF are thickened.

2.2 Earthquake Detection and Location Method

We apply the PALM architecture (Zhou et al., 2021) to build the microseismic catalog of XJF. PALM utilizes phase picking, association, location, and matched filter technique to automatically build a microseismic catalog. The whole architecture is composed of two parts:

(1) PAL: phase picking, association and location

PAL first detects candidate phases with short-term-average over long-term-average (STA/LTA) algorithm (Allen, 1978). The P & S arrivals are then picked in pairs by a hybrid picker incorporating STA/LTA and Kurtosis algorithm. In the phase association process, the estimated origin time on each station is clustered, and then a 3D grid search is applied to search for a location with the minimum travel time residual. For event location, we first apply HypoInverse (Klein, 2002) for absolute location, and then use HypoDD (Waldhauser and Ellsworth, 2000) to refine the relative location between events. For PAL detections in XJF, we employ the 1-D velocity model of Wang et al. (2002) (Figure S3) for both HypoInverse and HypoDD location. The stability of HypoInverse location result is tested with different velocity models (see Text S1). For HypoDD relocation, we set WDCT=30-km and apply 4 iterations, while other weighting schemes give similar results (see Text S1).

(2) MESS: matched filter, expand, time shift, and stacking

MESS is a modified matched filter detector that utilizes GPU for acceleration and provides cross-correlation (CC) measured differential times (i.e., *dt.cc* in hypoDD terminology) for high-resolution relocation. The MESS algorithm includes four steps in detection: 1) matched filter, where cross-correlation between continuous data and templates are calculated; 2) expand, where peaks on CC traces are expanded to allow for new detections away from templates; 3) time shift, where P wave travel times are shifted to align station records; and 4) stacking, where the expanded and shifted CC traces are stacked to suppress the noise level, based on which the detections are declared.

For MESS detections in XJF, we set the template window length as 1-s before and 11-s after P arrival, which covers both P and S wave. We set the minimum CC threshold for detection as 0.25. The P and S arrival times of detected events are then picked by waveform cross-correlation, but with a shorter window length to separate P & S wave: 0.5-s before to 2.5-s after the phase arrival. We input this high-resolution *dt.cc* into HypoDD (Waldhauser, 2001) for relocation. For XJF, we set WDCC=10-km with 1 iteration to relocate the MESS detected events. The stability of the relocation result is tested with different weighting schemes (see Text S2).

3. Results and Discussion

3.1 Microseismicity Locations and Fault Structure

The PALM detection method finally gives 12,881 well-located events during the study period from 2016-09 to 2019-01. Compare with the regional catalog provided by CSES, our PALM catalog gives much improved location accuracy and catalog completeness of the regional seismicity (Figure 3), which is due to the dense seismic network and the effectiveness of PALM algorithm. The PALM detection and location procedure is well-behaved in the XJF network: (1) the initial ~4,500 detections given

by PAL is augmented to ~13,000 by MESS, a ~2 times increase; (2) the location of PAL is stable and accurate under different velocity model and location parameters (Text S1); (3) the location results between PAL and MESS are consistent with each other, while MESS reveals more detailed image (Text S3); (4) the MESS catalog reach a lower magnitude of completeness than PAL, but with the same FMD for the complete part (Figure S10b).

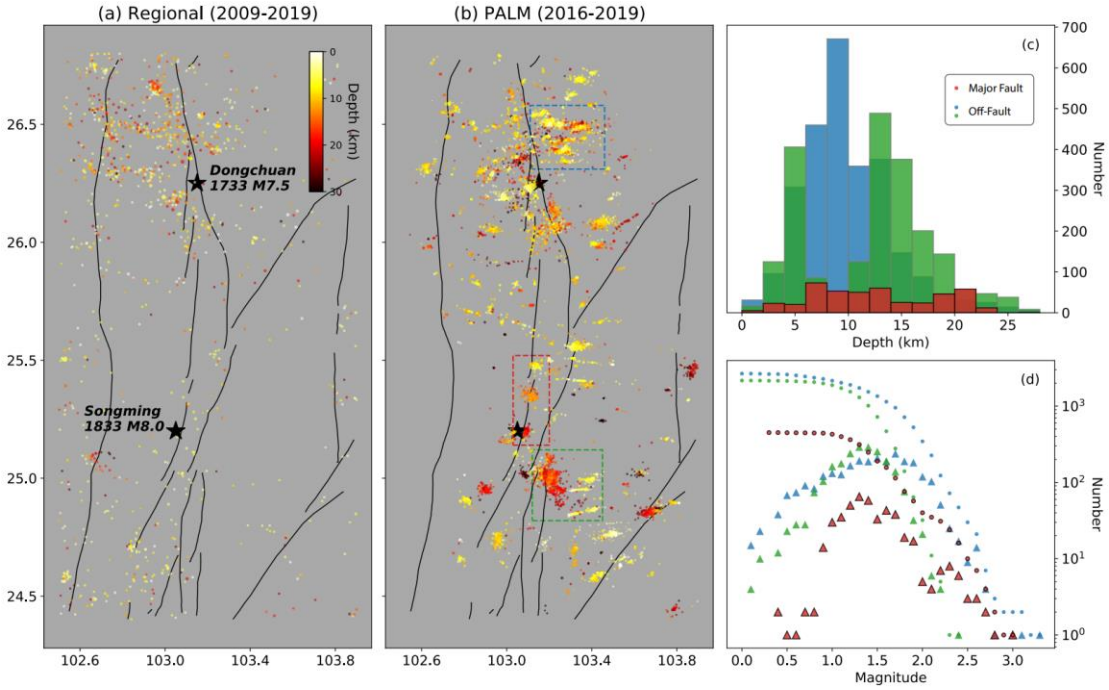

Figure 3. Detection and location result. (a) and (b) plot the CSES regional catalog during 2009 to 2019 and PALM catalog during 2016 to 2019, respectively. Earthquake epicenters are shown in dots that colored by depths. The black lines depict fault traces. Three areas (one on and off the major fault) are marked by red, blue and green dashed rectangles, whose depth distribution and frequency-magnitude distribution are plot in (c) and (d) respectively.

The microseismicity reveals abundant off-fault structures around XJF, which show clear lineation in the ENE-WSW direction, conjugating the main trend of the XJF (Figure 3,4). The seismic events on the main fault are highly clustered, with limited spatial lineation. Referring to a detailed fault mapping result from geological investigations, we find that the seismic clusters on the major fault occur on the intersections between the main fault and cross-cutting branches (Zhang and Xie, 2001; Shen et al., 2003). Such fault geometry is typical for a strike-slip fault system with subparallel branches, where conjugate faults and rhombus shaped sub-blocks are developed in between (Nicholson et al., 1986; Kilb and Rubin, 2002). Assuming that the deep micro-earthquakes occur on the junction between the main and conjugate faults, the dip angle of main fault branches can be determined in the fault vertical cross-sections (Figure 4d), which show a slightly east-dipping sub-vertical geometry.

The formation of the major XJF fault structure can be explained by the Riedel shear

theory (Ronald et al., 1973; Davis et al., 2000). At the initial stage, conjugate faults are formed at the preferred Coulomb failure orientation, forming *én* echelon faults (R shear) and conjugate faults (R' shear) in pairs on two side of the maximum compressional stress direction. The R and R' faults initially align in an acute angle, but with continuous shearing, the sub-blocks rotate and deform, changing it to an obtuse angle. For the XJF, the major branches (R shear) and the conjugate faults (R' shear) form an obtuse angle, which indicates that XJF is at a late stage of Riedel shear development (Nicholson et al., 1986; Kilb and Rubin, 2002).

In summary, the regional fault structure of XJF can be classified as two groups: (1) two sub-parallel NS trending major faults that show *én* echelon structure; and (2) several short conjugate faults between and off the major faults.

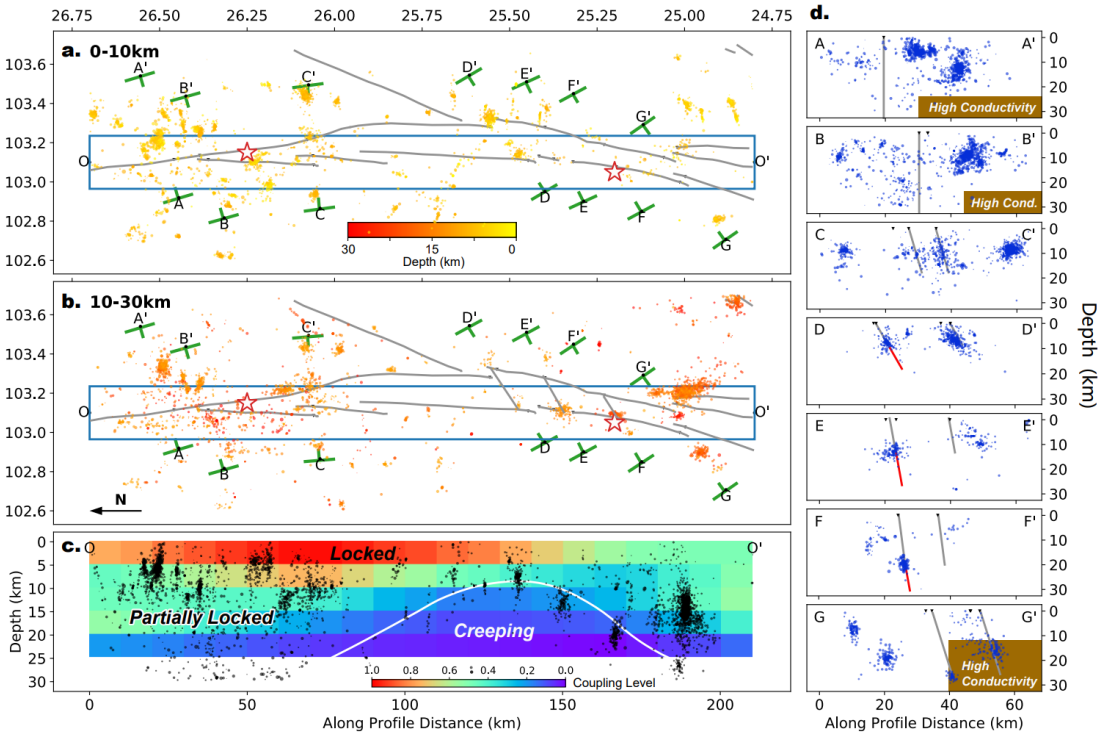

Figure 4. Seismicity pattern around XJF. (a) and (b) Map view of shallow (0-10km) and deep (10-30km) seismicity, respectively. Events are shown in dots colored by depths. Gray lines are fault traces. Blue rectangular and OO' mark the endpoints of the overall cross-section; Green frames from AA' to GG' mark the endpoints of the local cross-sections in (d). (c) and (d) plots overall and local cross-sections, where microseismic events are plotted as black and blue dots, respectively. Inter-seismic coupling ratio (ISC) from Li et al. (2021) is color-coded in (c). Vertical lines in (d) mark the dipping direction of the major fault. Fault zone conductors detected by Li et al. (2019) are marked by brown patches in (d).

3.2 Locking Pattern of the Major Fault

The spatial distribution of microseismicity also provides insights into slip behaviors. On the major Xiaojiang faults, the rather low microseismicity agrees with

the high locking ratio revealed by GPS measurements (Fang et al., 2005; Zhao et al., 2015; Fu et al., 2020). Such strong locking is more significant for the seismic quiescence segment in the seismic gap between the Songming and Dongchuan epicenter (from 25.5°N to 26°N) (Wen et al., 2008), which correlates well with the segment of large increase in cumulative Coulomb stress since 1713 (Shan et al., 2013). Similar quiescence of microseismicity on the major fault is also reported on the Alpine Fault of New Zealand, which is in the late stage of an earthquake cycle (Chamberlain et al., 2017).

On the western branch of XJF, we identified a special group of earthquake clusters with variable epicentral depths ranging from 25-km near 25°N to 10-km at 25.5°N (Figure 3b, 4c). Note that the XJF is currently at an interseismic period, we assume the seismic activity is mostly driven by fault creeps occurring at depth. Adopting a shear dislocation model with deep fault creep, the stress accumulation is concentrated at the boundary between creeping and locking patches, driving intense seismic activities (Jiang and Lapusta, 2017). Thus, in XJF, the spatial trend of deep seismic events is an indicator of the locking depth. In comparison with a recent interseismic locking model derived by geodetic data (Li et al., 2021), we find a good agreement between seismicity distribution and boundary of locking-creeping patches (Figure 4c). This correspondence between micro-seismicity location and the locking depth also applies to the Himalayan thrust front (Ader et al., 2012) and San Andreas Fault (Waldhauser et al., 2004; Wdowinski, 2009).

Overall, the strong locking of major Xiaojiang Fault is well supported by both GPS studies and a low seismic rate reported here. We will provide even more lines of evidence from repeater analysis (Section 3.3), temporal evolution of seismicity (Section 3.4), and b-value mapping (Section 3.5). However, the slip behavior of the off-fault structures is more difficult to revolve, on which we will show additional analysis on seismicity in Section 3.3-3.5 and make a concentrated discuss in Section 3.6.

3.3 Repeater Analysis

To investigate the slip behavior of subsidiary faults, we conducted repeating earthquake detection and analysis. As reviewed in Section 1.2, repeating earthquakes is usually considered as a re-rupturing of the same asperities driven by aseismic slips (Uchida and Bürgmann, 2019). The detection of repeaters requires strict criteria in both waveform similarity and location separation:

(1) High waveform similarity. We require a minimum cross-correlation threshold to be 0.9 for more than one station observation. The template window for cross-correlation is 10s-long (1-s before and 9-s after P arrival), covering both P and S waves. This is a relatively low threshold among other repeater studies (Uchida, 2019), but can tolerate the waveform difference caused by variation in noise level.

(2) Indistinguishable location difference. We measure the difference of S-P time on each station between a pair of events, and require a maximum deviation within 0.02s

for at least 3 stations. The S-P time is measured with cross-correlation, where P&S phase window if 2-s (0.5-s before and 1.5-s after P; 0-s before and 2-s after S) is applied. This operation avoids the uncertainty of clock error, since the operation is done on single stations.

Following the same clustering strategy in Text S3, we construct repeating sequences. The periodicity of sequence is analyzed with the coefficient of variation (COV) value of the recurrence interval, which is defined as the ratio of the standard deviation over the mean value of recurrent. A COV value of 0 corresponds to a purely periodic behavior, a COV value of 1 indicates a Poisson process, and COV > 1 suggests temporal clustering (Lengliné and Marsan, 2009; Li et al., 2011).

Results show that most repeaters occur on off-fault structures (Figure 6), which is consistent with the high coupling ratio of the major fault. The repeaters tend to occur in a random behavior (Figure 7a,b): the sequences' COV values range between 0.4 to 1.2, which deviates from a periodic recurrence pattern (COV=0) generated by isolated patch driven by constant aseismic slips. The high COV value indicates a temporal clustering of repeating earthquakes, which may be driven by slow-slip events with higher slip rate than background creeping. Moreover, the repeating sequences with a shorter duration show more quasi-periodic feature, while longer sequences have a higher degree of clustering (Figure 7b). This suggests that the short-term creep rate tends to be stable, but the long-term creep rate is influenced by episodic events.

It is worth noting that the magnitude of repeaters concentrates around M_L1.8 (Figure 7c), which is smaller than that in most other studies (Uchida, 2019; Uchida and Bürgmann, 2019). Such small event size makes it hard to determine whether the repeaters detected in this study are re-rupturing the same asperity. Thus, we only consider them as possible repeaters, which differ from the ordinary repeaters that indicate stable fault creeping behavior. This result show that the off-fault region of XJF is not freely creeping, but is partially locked to near surface, which agrees with the GPS-inversed locking model by Li et al. (2021) (Figure 4c). Similar near-repeating clusters are also detected in adjacent to the co-seismic rupture zone of 2020 M_w6.8 Sivrice earthquake that occur on the East Anatolian Fault (Konca et al., 2021) and on the Anza segment of San Jacinto Fault loaded by the afterslip of moderate earthquakes (Shaddox et al., 2021), both of which report near-repeating earthquakes that recurrent irregularly and with variable magnitude, but are associated with aseismic fault slip.

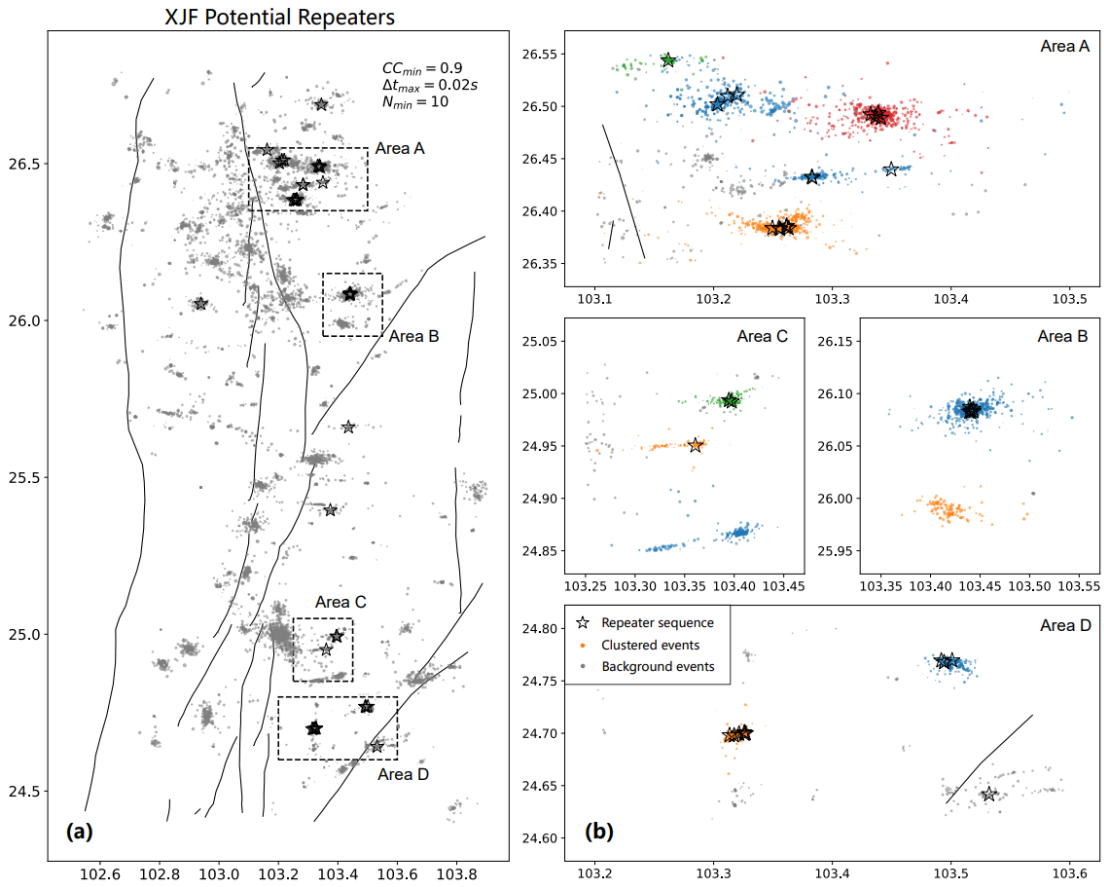

Figure 5. Distribution of repeating earthquakes. The left panel (a) is an overview of the whole region, and the right panels (b) show zoom-in plots of repeater distributions in the dashed boxes in (a). Locations of repeating sequences with more than 10 events are denoted by open stars. The colored events in (b) are clusters separated by waveform similarity analysis (see Text S3, Figure S11).

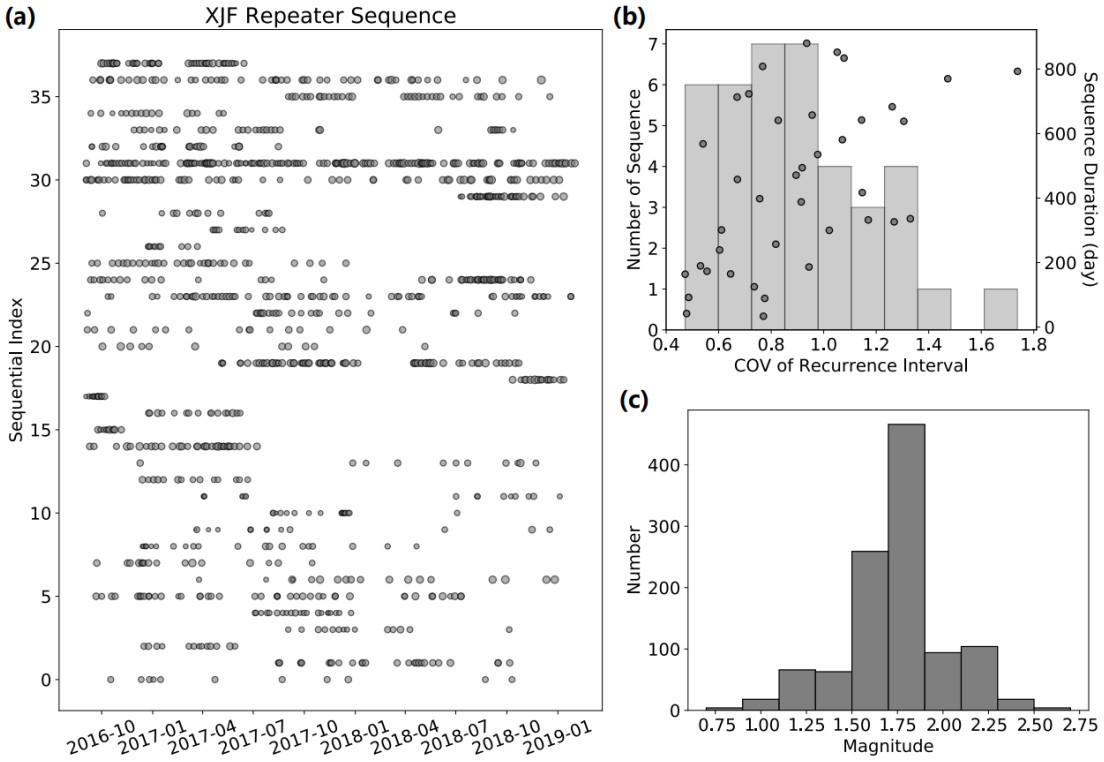

Figure 6. Repeating sequence analysis. (a) Repeating sequences. Horizontal and vertical axes are origin time and sequence index, respectively. Note that the sequence indexes are sorted by latitude. Gray dots denote repeating events, with the size proportional to the magnitude. (b) Periodicity of sequence. Histogram plots the number of sequences with respect to the COV value of recurrence interval. Gray dots mark the sequence duration and its COV value. (c) Histogram for the magnitude distribution of repeaters.

3.4 Temporal Evolution of Seismicity

We further analyze the temporal evolution of seismicity and the GPS time series to infer the slip behavior of off-fault structures. We first examine the seismicity rate in each separated area in Figure 5. We found that different seismic clusters in an area tend to be activated spontaneously (Figure 7), indicating that they are driven by the same mechanism. Note that each area is constituted by multiple faults and has a scale of 10-20km, which excludes the possibility of smaller-scale mechanisms, e.g. inter-event triggering, because the scale of seismicity clustering area is much larger than the stress influence area of such small events.

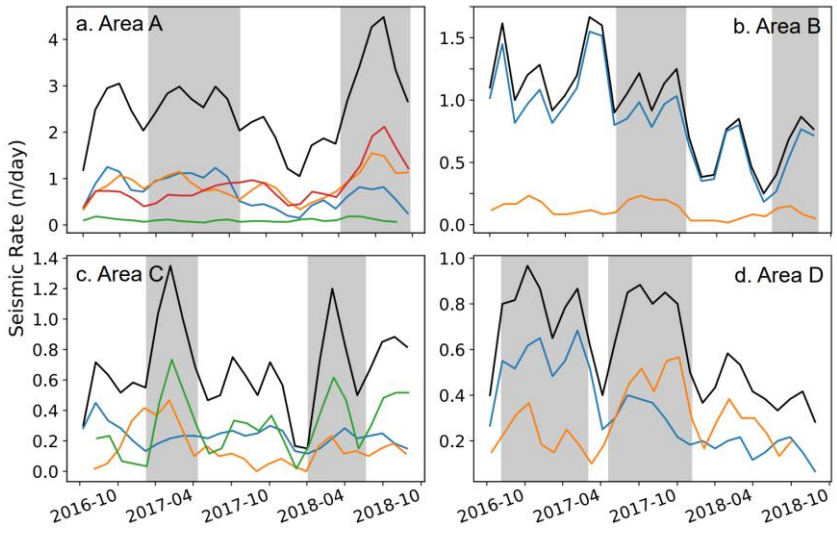

Figure 7. Temporal evolution of seismic rate in different area. The black and colored lines plot total and clustered seismic rate, with the color of different clusters the same as Figure 5. Gray patches mark the spontaneous active period of micro-seismicity in different clusters.

We collect displacement data of three continuous GPS stations on the northern XJF to further investigate the spatiotemporal deformation behavior of this area (Figure 2, 8a). The geometry of three stations are shown as Figure 8a: Station DTB locates at the west side of the XJF, while station HNG and HDH locates on the north and south side of the off-fault branches, respectively. The original data is processed with daily solution and reference to the whole earth coordinate. We subtract the solution of HDH from the other two stations to recover relative displacement across two fault structures: HDH-DTB reflects the deformation across the XJF, and HDH-HNG reflects the deformation across the off-fault structures. It is noted that such subtraction also removes the common mode errors in the original data.

Timeseries of relative displacements are plotted in figure 8b. It is evident that the most significant deformation in this area is the left-lateral shearing in the NS direction across the XJF at an averaged velocity of ~5 mm/yr. Deformation across the off-fault structures is dominated by right-lateral shearing in the EW direction at ~1mm/yr rate (figure 8b). Such sense of motion is consistent with the tectonic shear loading of the XJF, while it also indicates that the off-fault structures is undergoing slow right lateral sense of deformation.

The seismic rate is compared with the off-fault slip rate (figure 8c). We recover the relative velocity from daily slips and smooth the velocity with a 60-day running window. The seismicity rate for events above M_L2 in Area A is also smoothed with 60-day time windows. The comparison shows that the slip rates on the off-fault structures, though at a low rate, have a significant consistency with the seismicity rates (figure 8c). This consistency indicates a low fault strength, which may be caused by geothermal condition and high pore-pressure (Ake et al., 2005; Vidale and Shearer, 2006). Under the rate-state-dependent friction law, a high pore-pressure produce higher sensitivity

between shear stress and slip rates (Lu et al., 2021), therefore even small velocity change produces high shear stress change on these off-fault structure. At the same time, high pore pressure leads to low effective normal stress and low friction. If these structures are close to failing criterion, stress excess produced by velocity increase will increase seismic activities, which explains the temporal correlation between slip rates and seismicity rates.

Seismic activities on these off-fault structures, though intensive, cannot produce the observed slip rate (~1 mm/yr), thus extra aseismic creeping, maybe in a form of episodic creeps in the deep portions of off-fault branches, appears to be responsible for the synchronized seismic activities and surface deformation rates. We also processed SAR images to extract the cross-fault velocity gradients across these off-fault structures (Text S4). The solution reveals no significant deformation in the shallow part of these structures (figure S14). This observation indicates these structures are locked at the ground surface, while slowly creeping beneath the seismogenic depths (~20km).

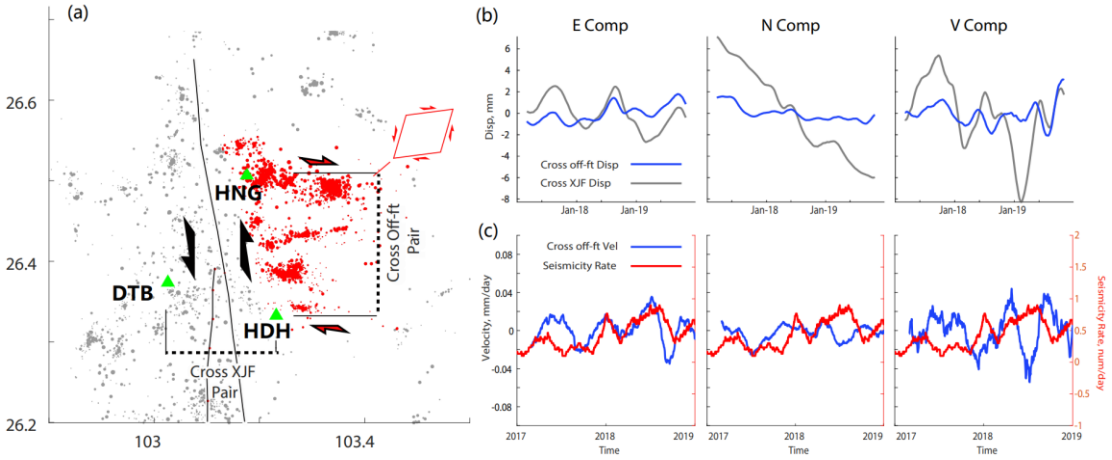

Figure 8. (a) Location of three GPS stations are denoted as green triangles. Earthquakes in background and off-fault structures are plotted as gray and red dots, respectively. (b) E, N and Vertical component of relative displacement across the XJF and off-fault branches are plotted as gray and blue curves, respectively. (c) E, N and V component of relative velocity across the off-fault structures are plotted as blue curves in each panel. Smoother seismicity rate in area A are plotted as red curves.

3.5 b-Value Mapping

We map the distribution of b-value to infer the stress variation along XJF region. As demonstrated in Section 1.2, the b-value in G-R law can be used to infer the stress status of natural fault. The G-R law states that the earthquake magnitude and its occurrence frequency follow a power-law distribution:

$$log_{10}N = a - b(M - M_c)\,, \tag{1}$$

where N is the number of events with a magnitude M or larger, M_c is the minimum magnitude of earthquake catalog completeness, and a and b are constants known as

the a-value and b-value. In mapping detailed b-value distribution, we define the magnitude of completeness M_c as the magnitude of maximum non-cumulative number of events, namely the maximum curvature method (MAXC, (Wiemer and Wyss, 2000):

$$N_{non-cum}(M_c) = N_{max}\,, \tag{2}$$

where $N_{non-cum}$ is the number of non-cumulative events, which is a function of magnitude, and N_{max} is the maximum of $N_{non-cum}$. Tests show that the MAXC method is stable for even small number of events, and is capable to reveal heterogeneous M_c and b-value distribution (Woessner and Wiemer, 2005; Zhou et al., 2018). The b-value is estimated by the maximum likelihood estimation (Aki, 1965):

$$b = \frac{log_{10}\, e}{\bar{M} - M_C + \Delta M/2}\,, \tag{3}$$

where $\bar{M}$ is the mean magnitude and ΔM is the width of the magnitude bin. The uncertainty of b-value estimation (δb) follows the widely adopted formula given by Shi and Bolt (1982):

$$\delta b = 2.3b^2 \sqrt{\sum_{i=1}^{n} \frac{(M_i - \bar{M})^2}{n(n-1)}}\,, \tag{4}$$

where n is the number of events.

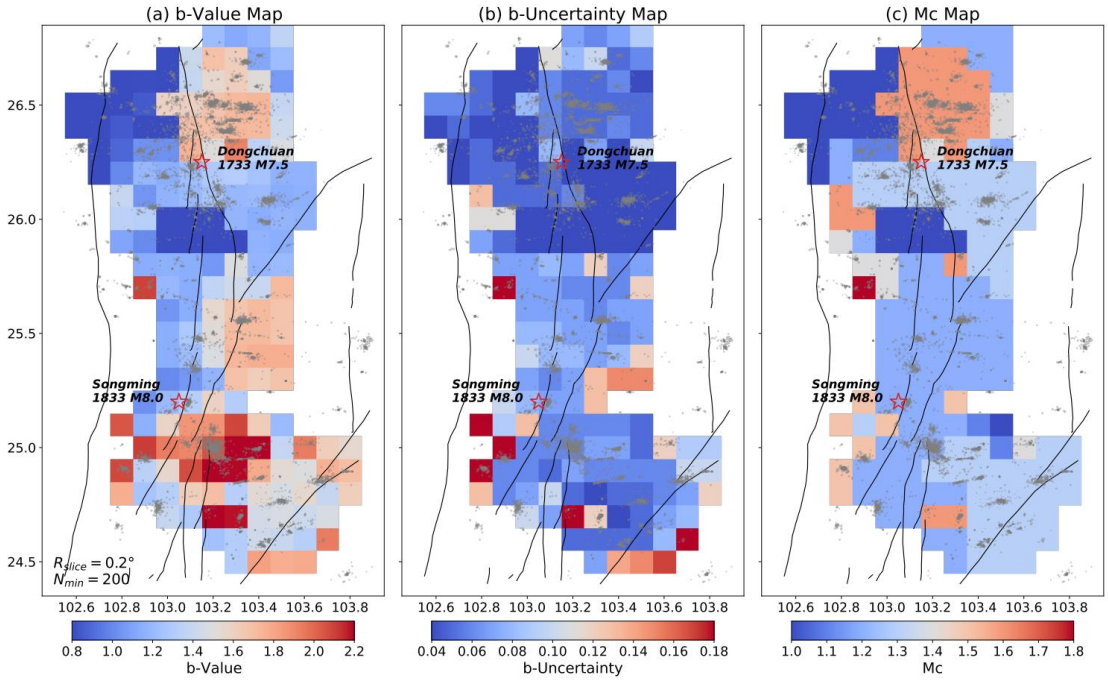

Figure 9. Maps of (a) b-value, (b) b-value uncertainty, and (c) magnitude of completeness Mc. Events and fault traces are plotted in gray dots and black lines, respectively. Red stars mark the epicenters of the 1733 and 1833 historical earthquakes.

We calculate b-value using the PALM catalog on each spatial grid. The grid spacing is set to 0.1°, and events within a radius of 0.2° are associated with each grid. We impose a minimum number of 200 as a number criterion for robust b-value estimation. A stability test is performed for different event association radii (Figure S15, S16). The

resulting b-map has complete coverage for the study region (Figure 9a), with an uncertainty below 0.1 for most grids (Figure 9b). The M_c ranges from M_L1.0~1.6 for most part of the region (Figure 9c), indicating high detection completeness.

On the main fault, the b-value is low along the seismic gap between the epicenter of 1733 Dongchuan and 1833 Songming earthquake (Figure 9a, (Wen et al., 2008; Ren, 2013), indicating high stress level. This low-b feature is consistent with the low seismic rate on the main fault (Section 3.1), which suggest strong fault coupling. The epicenter of Dongchuan and Songming earthquake lie in a transition region between high and low b-value (Figure 9a), which fit well with the spatial variation of interseismic fault coupling (Figure 4c, (Li et al., 2021). In contrast, the off-fault structures have significantly higher b-values (also see Figure 3d for example FMDs), which are commonly associated with a low stress level (El-Isa and Eaton, 2014) or weak fault strength (Scholz, 2015). Mechanisms related to weak fault strength include: (1) velocity strengthening frictional properties (Schurr et al., 2014), (2) low-effective normal stress (Bachmann et al., 2012), and (3) geothermal or volcanic conditions (Murru et al., 2007).

3.6 Locking Behavior and Strength of the Off-fault Structures

It is noted that the XJF is under an interseismic loading period, while the most intensive microseismicity are concentrated on off-fault structures, especially in two areas near 26.5°N and 25°N east of XJF. We infer geothermal condition of these two locations may be responsible for such high seismic activity, as indicated by high conductivity (Bai et al., 2010; Li et al., 2019) and distribution of hot springs (Shi and Wang, 2017). As analyzed in detail for the NE area of XJF, this area (1) shows strong correlation between seismicity and slip rate, (2) possibly hosts repeating earthquakes, and (3) are characterized by high b-value. Therefore, off-fault structures in this area may be subject to low-frictional strength and deep episodic slow-slip events.

Considering the deformation across the off-fault structures, as also the spatial decaying of NS shearing in the normal direction of XJF, the area with intensive off-fault structures is undergoing a right-lateral shearing in the NS direction and left lateral shearing in the EW direction (Figure 8a). Such mode of deformation is close to a pure-shear deformation within a bulk. Elastic theory supports that a pure-shear deformation in such a geometry setting releases shear direction in both NW and EW direction. As a volume of the eastern wall of XJF, shear stress loading is partially released by the distributed shearing in this volume. Thus, the shear stress on XJF near these geothermal areas should be lower in comparison with other strongly locked areas, and may serve as stress barriers for co-seismic ruptures. At the same time, geothermal portions of XJF may cause a velocity strengthening behavior because of a low effective normal stress. Recent observations of continental strike slips events show, the co-seismic ruptures can be terminated by geothermal conditions, e.g. the 2016 Kumamoto earthquake (Yagi et al., 2016; Yue et al., 2017) and 2019 Ridgecrest earthquake (Liu et al., 2019; Wang et al., 2020; Yue et al., 2021b). The spatial segmentation of historical events along the XJF,

e.g. Songming and Dongchuan earthquake, appears to be terminated by these two loci (Shen et al., 2003; Wen et al., 2008; Ren, 2013). Therefore, the fault portion between the 26° and 25.5°, may be an independent rupture segment bounded by geothermal portions on its two ends (Figure 9).

Considering the overall tectonic setting near the XJF, its west part shows distributed shear, with three extra NS trending sub-parallel faults, e.g. Luzhijiang fault, Yimen fault (YMF) and Puduhe fault (PDF), with ~30 km interval (Wang and Shen, 2020). The lower crust to the west side of XJF shows a low material strength, as validated by (1) a low P and S wave velocity in the lower crust (Wu et al., 2013; Bao et al., 2015; Yang et al., 2020), (2) a low-electric resistivity (Bai et al., 2010; Li et al., 2019), (3) a high attenuation (Zhao et al., 2013), (4) relatively high heat flow and concentrated hot springs (Shi and Wang, 2017), and (5) a high b-value (Figure 1b). Such low material strength may be generated by a radial active decay of a thick crust (~50 km) and shearing generated heat (Wang et al., 2017). Thus, we infer that a ductile lower crust with distributed shear deformation to the west side of XJF, and that all four large faults above the ductile zone are subject to a potential for large earthquakes. A similar shear pattern is also found for the Songpan-Ganze block near NE boundary of Tibetan plateau. Large earthquakes were found to occur within the shear zone instead of only on boundary faults (Yue et al., 2021a). Therefore, denser geodetic and seismic observation in this area are needed to evaluate the seismic hazard in the whole area.

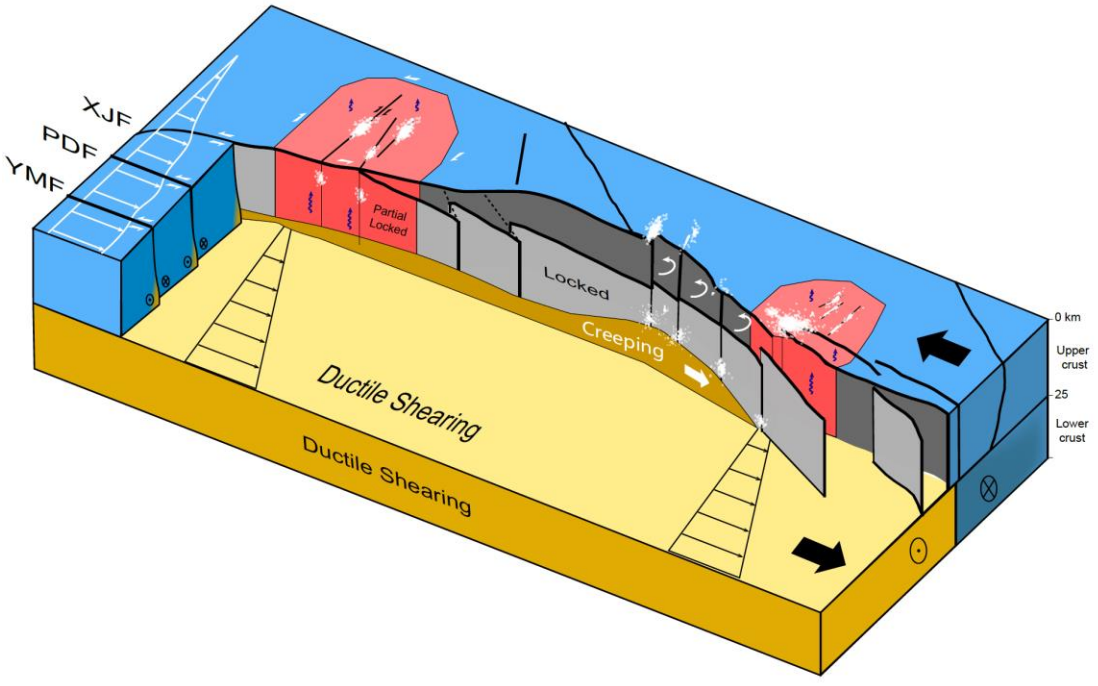

Figure 10. Conceptual model of XJF. Crust with different depth and different properties are separated by color. Faults traces and planes are plotted in black lines and gray patches. White dots plot characteristic seismic clusters. Black arrows mark the block motion.

3.7 Seismic Hazard of XJF

Based on the above discussions, we imaged the structure of XJF and demonstrated its slip behaviors (Figure 10). Here, we analyze the implications of such fault characteristics on the seismic hazard.

The major Xiaojiang fault is composed of several sub-faults aligned in an *én* echelon pattern. Historically, this ~150-km-long fault trace is capable to create M7-8 earthquakes (Shen et al., 2003; Wen et al., 2008; Ren, 2013; Li et al., 2015). To evaluate the current potential of XJF of generating large events, we suppose that a large earthquake requires a high stress level on a large scale, which has been validated by dynamic rupture simulations (Day, 1982; Wesnousky, 2008; Yang et al., 2019). In XJF, the quiescent segment between the Dongchuan and Songming epicenters (~25.5-26°N) fulfills such criteria: (1) the lowest b-value in the study area (Figure 8a); (2) the largest cumulative Coulomb stress change (1-10MPa) given by Shan et al. (2013); (3) the highest locking ratio along XJF inverted from GPS (Li et al., 2021). Thus, we conclude that this ~50-km-long gap is still susceptible for dynamic rupture, which can lead to a ~M7 earthquake if being completely ruptured.

The origin time of future large earthquake is especially hard to predict. In this discussion, we only consider which stage does XJF lie in the whole cycle. As stated in Section 1.1, the earthquake cycle given by paleo-seismic studies are not consistent with each other. We can revisit this problem by direct evidence from the fault slip rate and coseismic offset. Multiple GPS measurements over decades give a slip rate of 7-10 mm/yr on XJF (Shen et al., 2003; Shen et al., 2005; Wang et al., 2015; Fu et al., 2020). Adopting the field observation by Ren (2013), the coseismic offset of the 1833 Songming earthquake ranges from ~3-6m, which would lead to a maximum of 850-year recurrence interval, still much smaller than ~2000-year by Shen et al. (2003). On the other hand, the average interval is about 500 years following this estimation, which is comparable to 370-480 years given by Li et al. (2015). Thus, we prefer the paleo-earthquake result from Li et al. (2015), and infer that XJF is at its late stage of seismic cycle, considering the 200-300 years' elapse from the 1733 and 1833 event.

Besides, our b-value mapping result also solves the contradiction between the average b-value and geodetic estimation mentioned in Section 1.1: regional catalog gives high average b-value on XJF (Figure 1b), but geodetic estimation by Wang et al. (2015) gives high moment deficit. We interpret this phenomenon as the bias of average b-value: in XJF, the off-fault structures and regional distributed shear generate distributed microseismicity with high b-value, which lead to an overestimation of b-value on the major fault. If we use the b-value on major fault to represent the current stress level of XJF, the ~0.9 b-value (Figure 9a) is comparable to that on AZF and XSHF, which is consistent with geodetic results (Wang et al., 2015). Thus, in adopting the b-value inference, a high-completeness catalog with detailed b-mapping is important.

4. Conclusions

In this paper, we obtained a high-resolution image of microseismicity in XJF with a temporal seismic network and PALM detection method. Combining spatiotemporal feature of seismicity, repeater analysis, and b-value mapping, we characterize the behavior of XJF during its interseismic period. The main conclusions include:

(1) We found that the XJF is composed of two sets of structures: the two major branches and the conjugate sub-faults. The major Xiaojiang fault includes two sub-parallel NS-trending branches, each showing *én* echelon geometry. It is overall strongly locked, generating low microseismicity, low b-value, and no repeaters. The clusters on western branch show variable depth around the epicenter of 1833 Songming earthquake, delineating a fault segment with shallow locking depth.

(2) The off-fault structures form conjugate geometry with the main faults. The intense microseismicity on these sub-faults are driven by small fault slip, indicating stress loading released by distributed shear. We propose that such behavior may be caused by geothermal-induced fault weakening mechanism, which explains all observations in this and previous studies, including the potential repeating events, high b-value, and low resistivity at shallow depth. These distributed shearing area may serve as both stress and material barriers for future large earthquakes, which bound the segment of XJF between 25.0°N and 26.5°N as an isolated rupture segment.

(3) The overall b-value in the central of XJF is low, indicating a high stress level. Considering the locking pattern of XJF and its surrounding loading environment, we infer that XJF at a late stage of interseismic loading. The segment between 25.0°N and 26.5°N may be subject to an ~M7 earthquake in the future.

Acknowledgments

We thank Prof. Shiqing Xu for his suggestive discussion, Dr. Yanchuan Li for sharing the inter-seismic coupling model, and Dr. Yuexin Li for her validation on SAR image processing. Figures are plotted with GMT and Matplotlib. The detection and location software PALM is available on Github: PAL https://doi.org/10.5281/zenodo.5571290; MESS https://doi.org/10.5281/zenodo.5574634. The microseismic catalog of XJF is attached in the supporting materials. Catalog of historical earthquakes comes from the China Earthquake Networks Center, National Earthquake Data Center (http://data.earthquake.cn). Relocated regional catalog and focal mechanism solutions of the Sichuan-Yunnan region are provided by the China Seismic Experimental Site (CSES), at http://www.cses.ac.cn/. Data for fault traces and boundaries of tectonic blocks come from Deng et al. (2003a) and Zhang et al. (2003), respectively. This research is supported by the Nature Science Foundation of China (NSFC) projects (Grant Number 41774067 & U2039204 & 42074046 & U1939202), the National Key

R&D Program of China (2018YFC1503400), and the US National Science Foundation (award number 1941719).

References

Ader, T., et al. (2012). Convergence rate across the Nepal Himalaya and interseismic coupling on the Main Himalayan Thrust: Implications for seismic hazard, *Journal of Geophysical Research: Solid Earth*, *117*(B4), doi:10.1029/2011jb009071.

Ake, J., K. Mahrer, D. O'Connell, and L. Block (2005). Deep-Injection and Closely Monitored Induced Seismicity at Paradox Valley, Colorado, *Bulletin of the Seismological Society of America*, *95*(2), 664-683, doi:10.1785/0120040072.

Aki, K. (1965). Maximum likelihood estimate of b in the formula log N= a-bM and its confidence limits, *Bull. Earthq. Res. Inst., Tokyo Univ.*, *43*, 237-239.

Allen, R. V. (1978). Automatic earthquake recognition and timing from single traces, *Bulletin of the Seismological Society of America*, *68*(5), 1521-1532.

Bachmann, C. E., S. Wiemer, B. P. Goertz-Allmann, and J. Woessner (2012). Influence of pore-pressure on the event-size distribution of induced earthquakes, *Geophysical Research Letters*, *39*(9), doi:10.1029/2012gl051480.

Bai, D., et al. (2010). Crustal deformation of the eastern Tibetan plateau revealed by magnetotelluric imaging, *Nature Geoscience*, *3*(5), 358-362, doi:10.1038/ngeo830.

Bao, X., et al. (2015). Two crustal low-velocity channels beneath SE Tibet revealed by joint inversion of Rayleigh wave dispersion and receiver functions, *Earth and Planetary Science Letters*, *415*, 16-24, doi:https://doi.org/10.1016/j.epsl.2015.01.020.

Bender, B. (1983). Maximum likelihood estimation of b values for magnitude grouped data, *Bulletin of the Seismological Society of America*, *73*(3), 831-851.

Bürgmann, R., D. Schmidt, R. M. Nadeau, M. d'Alessio, E. Fielding, D. Manaker, T. V. McEvilly, and M. H. Murray (2000). Earthquake Potential Along the Northern Hayward Fault, California, *Science*, *289*(5482), 1178-1182, doi:10.1126/science.289.5482.1178.

Chamberlain, C. J., C. M. Boese, and J. Townend (2017). Cross-correlation-based detection and characterisation of microseismicity adjacent to the locked, late-interseismic Alpine Fault, South Westland, New Zealand, *Earth and Planetary Science Letters*, *457*, 63-72, doi:https://doi.org/10.1016/j.epsl.2016.09.061.

Chaussard, E., R. Bürgmann, H. Fattahi, C. W. Johnson, R. Nadeau, T. Taira, and I. Johanson (2015). Interseismic coupling and refined earthquake potential on the Hayward-Calaveras fault zone, *Journal of Geophysical Research: Solid Earth*, *120*(12), 8570-8590, doi:10.1002/2015jb012230.

Chen, K. H., R. Bürgmann, R. M. Nadeau, T. Chen, and N. Lapusta (2010). Postseismic variations in seismic moment and recurrence interval of repeating earthquakes, *Earth and Planetary Science Letters*, *299*(1), 118-125, doi:https://doi.org/10.1016/j.epsl.2010.08.027.

Davis, G. H., A. P. Bump, P. E. Garcı´a, and S. G. Ahlgren (2000). Conjugate Riedel deformation band shear zones, *Journal of Structural Geology*, *22*(2), 169-190,

627 doi:https://doi.org/10.1016/S0191-8141(99)00140-6.
628 Day, S. M. (1982). Three-dimensional simulation of spontaneous rupture: The effect of nonuniform
629 prestress, *Bulletin of the Seismological Society of America*, *72*(6A), 1881-1902,
630 doi:10.1785/bssa07206a1881.
631 Deng, Q., P. Zhang, Y. Ran, X. Yang, W. Min, and L. Chen (2003a). Active tectonics and earthquake
632 activities in China, *Earth Science Frontiers*(S1), 66-73.
633 Deng, Q., P. Zhang, Y. Ran, X. Yang, W. Min, and Q. Chu (2003b). Basic characteristics of active
634 tectonics of China, *Science in China Series D-Earth Sciences*, *46*(1006-9313), 356,
635 doi:https://doi.org/10.1360/03yd9032.
636 El-Isa, Z. H., and D. W. Eaton (2014). Spatiotemporal variations in the b-value of earthquake
637 magnitude–frequency distributions: Classification and causes, *Tectonophysics*, *615-616*,
638 1-11, doi:https://doi.org/10.1016/j.tecto.2013.12.001.
639 Fang, Y., Z. Jiang, and A. Niu (2005). Analysis of Crustal Deformation in East Boundary of Sichuan-
640 Yunnan Block, *Journal of Geodesy and Geodynamics*(03), 81-85.
641 Fu, Z., L. Xu, and Y. Wang (2020). Seismic Risk on the Northern Xiaojiang Fault Implied by the Latest
642 and Nearest GPS Observations, *Pure and Applied Geophysics*, *177*(2), 661-679,
643 doi:10.1007/s00024-019-02347-5.
644 Ghosh, A., A. V. Newman, A. M. Thomas, and G. T. Farmer (2008). Interface locking along the
645 subduction megathrust from b-value mapping near Nicoya Peninsula, Costa Rica,
646 *Geophysical Research Letters*, *35*(1), doi:https://doi.org/10.1029/2007GL031617.
647 Gulia, L., A. P. Rinaldi, T. Tormann, G. Vannucci, B. Enescu, and S. Wiemer (2018). The Effect of a
648 Mainshock on the Size Distribution of the Aftershocks, *Geophysical Research Letters*,
649 *45*(24), 13,277-213,287, doi:https://doi.org/10.1029/2018GL080619.
650 Gulia, L., and S. Wiemer (2019). Real-time discrimination of earthquake foreshocks and aftershocks,
651 *Nature*, *574*(7777), 193-199, doi:10.1038/s41586-019-1606-4.
652 Gutenberg, B., and C. F. Richter (1944). Frequency of earthquakes in California, *Bulletin of the*
653 *Seismological Society of America*, *34*(4), 185-188.
654 Jiang, J., and N. Lapusta (2017). Connecting depth limits of interseismic locking, microseismicity,
655 and large earthquakes in models of long-term fault slip, *Journal of Geophysical Research:*
656 *Solid Earth*, *122*(8), 6491-6523, doi:https://doi.org/10.1002/2017JB014030.
657 Kilb, D., and A. M. Rubin (2002). Implications of diverse fault orientations imaged in relocated
658 aftershocks of the Mount Lewis, ML 5.7, California, earthquake, *Journal of Geophysical*
659 *Research: Solid Earth*, *107*(B11), ESE 5-1-ESE 5-17, doi:10.1029/2001jb000149.
660 Klein, F. W. (2002). User's guide to HYPOINVERSE-2000, a Fortran program to solve for earthquake
661 locations and magnitudes*Rep. 2331-1258*, US Geological Survey.
662 Konca, A. Ö., H. Karabulut, S. E. Güvercin, F. Eskiköy, S. Özarpacı, A. Özdemir, M. Floyd, S. Ergintav,
663 and U. Doğan (2021). From Interseismic Deformation With Near-Repeating Earthquakes
664 to Co-Seismic Rupture: A Unified View of the 2020 Mw6.8 Sivrice (Elazığ) Eastern Turkey
665 Earthquake, *Journal of Geophysical Research: Solid Earth*, *126*(10), e2021JB021830,
666 doi:https://doi.org/10.1029/2021JB021830.
667 Lengliné, O., and D. Marsan (2009). Inferring the coseismic and postseismic stress changes caused
668 by the 2004 Mw = 6 Parkfield earthquake from variations of recurrence times of

669 microearthquakes, *Journal of Geophysical Research: Solid Earth*, *114*(B10),
670 doi:10.1029/2008jb006118.
671 Li, L., Q.-f. Chen, F. Niu, and J. Su (2011). Deep slip rates along the Longmen Shan fault zone
672 estimated from repeating microearthquakes, *Journal of Geophysical Research: Solid Earth*,
673 *116*(B9), doi:10.1029/2011jb008406.
674 Li, X., Y. Ran, L. Chen, F. Wu, X. Ma, and J. Cao (2015). Late Quaternary Large Earthquakes on the
675 Western Branch of the Xiaojiang Fault and Their Tectonic Implications, *Acta Geologica*
676 *Sinica - English Edition*, *89*(5), 1516-1530, doi:10.1111/1755-6724.12561.
677 Li, X., D. Bai, X. Ma, Y. Chen, I. M. Varentsov, G. Xue, S. Xue, and I. Lozovsky (2019). Electrical
678 resistivity structure of the Xiaojiang strike-slip fault system (SW China) and its tectonic
679 implications, *Journal of Asian Earth Sciences*, *176*, 57-67,
680 doi:https://doi.org/10.1016/j.jseaes.2019.01.031.
681 Li, Y., J.-M. Nocquet, X. Shan, and H. Jian (2021). Heterogeneous interseismic coupling along the
682 Xianshuihe-Xiaojiang fault system, eastern Tibet, *Journal of Geophysical Research: Solid*
683 *Earth*, *n/a*(n/a), e2020JB021187, doi:https://doi.org/10.1029/2020JB021187.
684 Liu, C., T. Lay, E. E. Brodsky, K. Dascher-Cousineau, and X. Xiong (2019). Coseismic Rupture Process
685 of the Large 2019 Ridgecrest Earthquakes From Joint Inversion of Geodetic and
686 Seismological Observations, *Geophysical Research Letters*, *46*(21), 11820-11829,
687 doi:https://doi.org/10.1029/2019GL084949.
688 Liu, J., L. Zhang, and Y. Du (2020). Seismic Hazard Assessment of the Mid-Northern Segment of
689 Xiaojiang Fault Zone in Southwestern China Using Scenario Earthquakes, *Bulletin of the*
690 *Seismological Society of America*, *110*(3), 1191-1210, doi:10.1785/0120190248.
691 Lu, W., Y. Zhou, Z. Zhao, H. Yue, and S. Zhou (2021). Aftershock sequence of the 2017 Mw 6.5
692 Jiuzhaigou, China earthquake monitored by an AsA network and its implication to fault
693 structures and strength, *Geophysical Journal International*, *228*(3), 1763-1779,
694 doi:10.1093/gji/ggab443.
695 Marzocchi, W., I. Spassiani, A. Stallone, and M. Taroni (2019). How to be fooled searching for
696 significant variations of the b-value, *Geophysical Journal International*, *220*(3), 1845-1856,
697 doi:10.1093/gji/ggz541.
698 Melgar, D., X. Pérez-Campos, L. Ramirez-Guzman, Z. Spica, V. H. Espíndola, W. C. Hammond, and
699 E. Cabral-Cano (2018). Bend Faulting at the Edge of a Flat Slab: The 2017 Mw7.1 Puebla-
700 Morelos, Mexico Earthquake, *Geophysical Research Letters*, *45*(6), 2633-2641,
701 doi:https://doi.org/10.1002/2017GL076895.
702 Mendoza, M. M., A. Ghosh, M. S. Karplus, S. L. Klemperer, S. N. Sapkota, L. B. Adhikari, and A.
703 Velasco (2019). Duplex in the Main Himalayan Thrust illuminated by aftershocks of the
704 2015 Mw 7.8 Gorkha earthquake, *Nature Geoscience*, *12*(12), 1018-1022,
705 doi:10.1038/s41561-019-0474-8.
706 Mori, J., and R. E. Abercrombie (1997). Depth dependence of earthquake frequency-magnitude
707 distributions in California: Implications for rupture initiation, *Journal of Geophysical*
708 *Research: Solid Earth*, *102*(B7), 15081-15090, doi:10.1029/97jb01356.
709 Murru, M., R. Console, G. Falcone, C. Montuori, and T. Sgroi (2007). Spatial mapping of the b value
710 at Mount Etna, Italy, using earthquake data recorded from 1999 to 2005, *Journal of*

Geophysical Research: Solid Earth, *112*(B12), doi:https://doi.org/10.1029/2006JB004791.

Nicholson, C., L. Seeber, P. Williams, and L. R. Sykes (1986). Seismic evidence for conjugate slip and block rotation within the San Andreas Fault System, southern California, *Tectonics*, *5*(4), 629-648, doi:10.1029/TC005i004p00629.

Ren, Z. (2013). Geometry and deformation features of the most recent co-seismic surface ruptures along the Xiaojiang Fault and its tectonic implications for the Tibetan Plateau, *Journal of Asian Earth Sciences*, *77*, 21-30, doi:https://doi.org/10.1016/j.jseaes.2013.08.016.

Ronald, E. W., T. P. Harding, and D. R. Seely (1973). Basic Wrench Tectonics, *AAPG Bulletin*, *57*(1), 74-96, doi:10.1306/819a424a-16c5-11d7-8645000102c1865d.

Scholz, C. H. (1968). The frequency-magnitude relation of microfracturing in rock and its relation to earthquakes, *Bulletin of the Seismological Society of America*, *58*(1), 399-415.

Scholz, C. H. (2015). On the stress dependence of the earthquake b value, *Geophysical Research Letters*, *42*(5), 1399-1402, doi:10.1002/2014gl062863.

Schorlemmer, D., and S. Wiemer (2005). Microseismicity data forecast rupture area, *Nature*, *434*(7037), 1086-1086, doi:10.1038/4341086a.

Schorlemmer, D., S. Wiemer, and M. Wyss (2005). Variations in earthquake-size distribution across different stress regimes, *Nature*, *437*(7058), 539-542, doi:10.1038/nature04094.

Schurr, B., et al. (2014). Gradual unlocking of plate boundary controlled initiation of the 2014 Iquique earthquake, *Nature*, *512*(7514), 299-302, doi:10.1038/nature13681.

Shaddox, H. R., S. Y. Schwartz, and N. M. Bartlow (2021). Afterslip and Spontaneous Aseismic Slip on the Anza Segment of the San Jacinto Fault Zone, Southern California, *Journal of Geophysical Research: Solid Earth*, *126*(6), e2020JB020460, doi:https://doi.org/10.1029/2020JB020460.

Shan, B., X. Xiong, R. Wang, Y. Zheng, and S. Yang (2013). Coulomb stress evolution along Xianshuihe–Xiaojiang Fault System since 1713 and its interaction with Wenchuan earthquake, May 12, 2008, *Earth and Planetary Science Letters*, *377-378*, 199-210, doi:https://doi.org/10.1016/j.epsl.2013.06.044.

Shelly, D. R., W. L. Ellsworth, and D. P. Hill (2016). Fluid-faulting evolution in high definition: Connecting fault structure and frequency-magnitude variations during the 2014 Long Valley Caldera, California, earthquake swarm, *Journal of Geophysical Research: Solid Earth*, *121*(3), 1776-1795, doi:10.1002/2015jb012719.

Shen, J., and Y. Wang (1999). Estimation of Seismic Risk of the Xiaojiang Active Fault Zone Using Slip Rate, *Journal of Seismological Research*(03), 251-259.

Shen, J., Y. Wang, and F. Song (2003). Characteristics of the active Xiaojiang fault zone in Yunnan, China: a slip boundary for the southeastward escaping Sichuan–Yunnan Block of the Tibetan Plateau, *Journal of Asian Earth Sciences*, *21*(10), 1085-1096, doi:https://doi.org/10.1016/S1367-9120(02)00185-2.

Shen, Z.-K., J. Lü, M. Wang, and R. Bürgmann (2005). Contemporary crustal deformation around the southeast borderland of the Tibetan Plateau, *Journal of Geophysical Research: Solid Earth*, *110*(B11), doi:10.1029/2004jb003421.

Shi, Y., and B. A. Bolt (1982). The standard error of the magnitude-frequency b value, *Bulletin of*

753 *the Seismological Society of America*, *72*(5), 1677-1687.
754 Shi, Z., and G. Wang (2017). Evaluation of the permeability properties of the Xiaojiang Fault Zone
755 using hot springs and water wells, *Geophysical Journal International*, *209*(3), 1526-1533,
756 doi:10.1093/gji/ggx113.
757 Spada, M., T. Tormann, S. Wiemer, and B. Enescu (2013). Generic dependence of the frequency-
758 size distribution of earthquakes on depth and its relation to the strength profile of the
759 crust, *Geophysical Research Letters*, *40*(4), 709-714, doi:10.1029/2012gl054198.
760 Sun, J., H. Yue, Z. Shen, L. Fang, Y. Zhan, and X. Sun (2018). The 2017 Jiuzhaigou Earthquake: A
761 Complicated Event Occurred in a Young Fault System, *Geophysical Research Letters*, *45*(5),
762 2230-2240, doi:10.1002/2017gl076421.
763 Templeton, D. C., R. M. Nadeau, and R. Bürgmann (2009). Distribution of postseismic slip on the
764 Calaveras fault, California, following the 1984 M6.2 Morgan Hill earthquake, *Earth and*
765 *Planetary Science Letters*, *277*(1), 1-8, doi:https://doi.org/10.1016/j.epsl.2008.09.024.
766 Tormann, T., S. Wiemer, and A. Mignan (2014). Systematic survey of high-resolution b value
767 imaging along Californian faults: Inference on asperities, *Journal of Geophysical Research:*
768 *Solid Earth*, *119*(3), 2029-2054, doi:10.1002/2013jb010867.
769 Uchida, N., J. Nakajima, A. Hasegawa, and T. Matsuzawa (2009). What controls interplate coupling?:
770 Evidence for abrupt change in coupling across a border between two overlying plates in
771 the NE Japan subduction zone, *Earth and Planetary Science Letters*, *283*(1), 111-121,
772 doi:https://doi.org/10.1016/j.epsl.2009.04.003.
773 Uchida, N., and T. Matsuzawa (2011). Coupling coefficient, hierarchical structure, and earthquake
774 cycle for the source area of the 2011 off the Pacific coast of Tohoku earthquake inferred
775 from small repeating earthquake data, *Earth, Planets and Space*, *63*(7), 30,
776 doi:10.5047/eps.2011.07.006.
777 Uchida, N. (2019). Detection of repeating earthquakes and their application in characterizing slow
778 fault slip, *Progress in Earth and Planetary Science*, *6*(1), 40, doi:10.1186/s40645-019-
779 0284-z.
780 Uchida, N., and R. Bürgmann (2019). Repeating Earthquakes, *Annual Review of Earth and Planetary*
781 *Sciences*, *47*(1), 305-332, doi:10.1146/annurev-earth-053018-060119.
782 Vidale, J. E., and P. M. Shearer (2006). A survey of 71 earthquake bursts across southern California:
783 Exploring the role of pore fluid pressure fluctuations and aseismic slip as drivers, *Journal*
784 *of Geophysical Research: Solid Earth*, *111*(B5), doi:https://doi.org/10.1029/2005JB004034.
785
786 Waldhauser, F., and W. L. Ellsworth (2000). A Double-Difference Earthquake Location Algorithm:
787 Method and Application to the Northern Hayward Fault, California, *Bulletin of the*
788 *Seismological Society of America*, *90*(6), 1353-1368, doi:10.1785/0120000006.
789 Waldhauser, F. (2001). hypoDD--A program to compute double-difference hypocenter locations,
790 *U.S. Geological Survey Open-File Report 01-113*, 25 pp.
791 Waldhauser, F., and W. L. Ellsworth (2002). Fault structure and mechanics of the Hayward Fault,
792 California, from double-difference earthquake locations, *Journal of Geophysical Research:*
793 *Solid Earth*, *107*(B3), ESE 3-1-ESE 3-15, doi:10.1029/2000jb000084.
794 Waldhauser, F., W. L. Ellsworth, D. P. Schaff, and A. Cole (2004). Streaks, multiplets, and holes:

High-resolution spatio-temporal behavior of Parkfield seismicity, *Geophysical Research Letters*, *31*(18), doi:10.1029/2004gl020649.

Wang, C., W.D.Mooney, X. Wang, J. Wu, H. Lou, and F. Wang (2002). Study on 3-D Velocity Structure of Crust and Upper Mantle in Sichuan-Yunnan Region, China, *Acta Seismological Sinica*(01), 1-16.

Wang, F., M. Wang, Y. Wang, and Z.-K. Shen (2015). Earthquake potential of the Sichuan-Yunnan region, western China, *Journal of Asian Earth Sciences*, *107*, 232-243, doi:https://doi.org/10.1016/j.jseaes.2015.04.041.

Wang, H., M. Liu, J. Cao, X. Shen, and G. Zhang (2011). Slip rates and seismic moment deficits on major active faults in mainland China, *Journal of Geophysical Research: Solid Earth*, *116*(B2), doi:10.1029/2010jb007821.

Wang, K., D. S. Dreger, E. Tinti, R. Bürgmann, and T. a. Taira (2020). Rupture Process of the 2019 Ridgecrest, California Mw 6.4 Foreshock and Mw 7.1 Earthquake Constrained by Seismic and Geodetic Data, *Bulletin of the Seismological Society of America*, *110*(4), 1603-1626, doi:10.1785/0120200108.

Wang, M., and Z.-K. Shen (2020). Present-Day Crustal Deformation of Continental China Derived From GPS and Its Tectonic Implications, *Journal of Geophysical Research: Solid Earth*, *125*(2), e2019JB018774, doi:10.1029/2019jb018774.

Wang, W., J. Wu, L. Fang, G. Lai, and Y. Cai (2017). Crustal thickness and Poisson's ratio in southwest China based on data from dense seismic arrays, *Journal of Geophysical Research: Solid Earth*, *122*(9), 7219-7235, doi:10.1002/2017jb013978.

Wdowinski, S. (2009). Deep creep as a cause for the excess seismicity along the San Jacinto fault, *Nature Geoscience*, *2*(12), 882-885, doi:10.1038/ngeo684.

Wen, X.-z., S.-l. Ma, X.-w. Xu, and Y.-n. He (2008). Historical pattern and behavior of earthquake ruptures along the eastern boundary of the Sichuan-Yunnan faulted-block, southwestern China, *Physics of the Earth and Planetary Interiors*, *168*(1), 16-36, doi:https://doi.org/10.1016/j.pepi.2008.04.013.

Wesnousky, S. G. (2008). Displacement and Geometrical Characteristics of Earthquake Surface Ruptures: Issues and Implications for Seismic-Hazard Analysis and the Process of Earthquake Rupture, *Bulletin of the Seismological Society of America*, *98*(4), 1609-1632, doi:10.1785/0120070111.

Wiemer, S., and M. Wyss (1997). Mapping the frequency-magnitude distribution in asperities: An improved technique to calculate recurrence times?, *Journal of Geophysical Research: Solid Earth*, *102*(B7), 15115-15128, doi:10.1029/97jb00726.

Wiemer, S., and M. Wyss (2000). Minimum Magnitude of Completeness in Earthquake Catalogs: Examples from Alaska, the Western United States, and Japan, *Bulletin of the Seismological Society of America*, *90*(4), 859-869, doi:10.1785/0119990114.

Woessner, J., and S. Wiemer (2005). Assessing the Quality of Earthquake Catalogues: Estimating the Magnitude of Completeness and Its Uncertainty, *Bulletin of the Seismological Society of America*, *95*(2), 684-698, doi:10.1785/0120040007.

Wu, J., T. Yang, W. Wang, Y. Ming, and T. Zhang (2013). Three dimensional P-wave velocity structure around Xiaojiang fault system and its tectonic implications, *Chinese Journal Of*

Geophysics, *56*(7), 2257-2267, doi:10.6038/cjg20130713.

Wu, Z., X. Zhang, and K. Sun (2019). China Seismic Experiment Site: scientific challenges, *Acta Geologica Sinica - English Edition*, *93*(S1), 273-273, doi:10.1111/1755-6724.14084.

Wyss, M., D. Schorlemmer, and S. Wiemer (2000). Mapping asperities by minima of local recurrence time: San Jacinto-Elsinore fault zones, *Journal of Geophysical Research: Solid Earth*, *105*(B4), 7829-7844, doi:10.1029/1999jb900347.

Yagi, Y., R. Okuwaki, B. Enescu, A. Kasahara, A. Miyakawa, and M. Otsubo (2016). Rupture process of the 2016 Kumamoto earthquake in relation to the thermal structure around Aso volcano, *Earth, Planets and Space*, *68*(1), 118, doi:10.1186/s40623-016-0492-3.

Yang, H., S. Yao, B. He, A. V. Newman, and H. Weng (2019). Deriving Rupture Scenarios From Interseismic Locking Distributions Along the Subduction Megathrust, *Journal of Geophysical Research: Solid Earth*, *124*(10), 10376-10392, doi:10.1029/2019jb017541.

Yang, Y., S. Hu, H. Yao, L. Fang, and J. Wu (2020). Crustal shear wave velocity and radial anisotropy in the Xiaojiang fault zone system (SE Tibet) revealed by ambient noise interferometry, *Tectonophysics*, *792*, 228594, doi:https://doi.org/10.1016/j.tecto.2020.228594.

Yue, H., Z. E. Ross, C. Liang, S. Michel, H. Fattahi, E. Fielding, A. Moore, Z. Liu, and B. Jia (2017). The 2016 Kumamoto Mw = 7.0 Earthquake: A Significant Event in a Fault–Volcano System, *Journal of Geophysical Research: Solid Earth*, *122*(11), 9166-9183, doi:10.1002/2017jb014525.

Yue, H., Z.-K. Shen, Z. Zhao, T. Wang, L. Zhao, and X. Song (2021a). A distributed shear zone near the northern margin of the Tibetan Plateau accommodates plateau expansion and growth, *(submitted)*.

Yue, H., J. Sun, M. Wang, Z. Shen, M. Li, L. Xue, W. Lu, Y. Zhou, C. Ren, and T. Lay (2021b). The 2019 Ridgecrest, California earthquake sequence: Evolution of seismic and aseismic slip on an orthogonal fault system, *Earth and Planetary Science Letters*, *570*, 117066, doi:https://doi.org/10.1016/j.epsl.2021.117066.

Zhang, P., Q. Deng, G. Zhang, J. Ma, W. Gan, W. Min, F. Mao, and Q. Wang (2003). Active tectonic blocks and strong earthquakes in the continent of China, *Science in China Series D: Earth Sciences*, *46*(2), 13-24, doi:10.1360/03dz0002.

Zhang, S., and F. Xie (2001). Seismo-Tectonic Divisions of Strong Earthquakes (MS>=7.0) and Their Tectonic Geomorphology along Xianshuihe-Xiaojiang Fault Zone, *Acta Seismologica Sinica*(01), 36-44+111.

Zhao, J., Z. Jiang, A. Niu, J. Liu, Y. Wu, W. Wei, X. Liu, and W. Yan (2015). Study on dynamic characteristics of fault locking and fault slip deficit in the eastern boundary of the Sichuan-Yunnan rhombic block, *Chinese Journal Of Geophysics*, *58*(03), 872-885, doi:10.6038/cjg20150316.

Zhao, L.-F., X.-B. Xie, J.-K. He, X. Tian, and Z.-X. Yao (2013). Crustal flow pattern beneath the Tibetan Plateau constrained by regional Lg-wave Q tomography, *Earth and Planetary Science Letters*, *383*, 113-122, doi:https://doi.org/10.1016/j.epsl.2013.09.038.

Zhou, Y., S. Zhou, and J. Zhuang (2018). A test on methods for MC estimation based on earthquake catalog, *Earth and Planetary Physics*, *2*(2), 150-162, doi:10.26464/epp2018015.

879 Zhou, Y., H. Yue, L. Fang, S. Zhou, L. Zhao, and A. Ghosh (2021). An Earthquake Detection and
880 Location Architecture for Continuous Seismograms: Phase Picking, Association, Location,
881 and Matched Filter (PALM), *Seismological Research Letters*, doi:10.1785/0220210111.
882
883